# Estimating Ocean Coherence Time using Dual-Baseline Interferometric Synthetic Aperture Radar

Richard E. Carande

*Jet Propulsion Laboratory*

*California Institute of Technology*

*Mail Stop 300--243*

*4800 Oak Grove Drive*

*Pasadena, CA 91109*

*Phone (818) 354-6720*

*FAX (818) 3936943*

Submitted to IEEE Transactions on Geoscience and Remote Sensing.

Date Submitted: March 1993

## ABSTRACT

A new technique for measuring the coherence time of the ocean surface at radar wavelengths has been developed and tested. This technique requires an interferometric synthetic aperture radar system with at least two unique baselines along the direction of platform motion. The coherence time of the surface may be presented as a high resolution coherence time map. In addition to the coherence time, the interferometric SAR information also provides the radar backscatter and mean Doppler shift for each pixel of the coherence time map.

This technique was tested using the JPL AIRSAR along-track interferometer. Measurements of the ocean coherence at L and C bands were made at high spatial resolution under a variety of conditions. Fundamental to this measurement is the ability of the AIRSAR system to image the ocean interferometrically at two different baselines, A new operating technique which allows this is described in here. Some parametric analysis is performed pertaining to the design of such a system. An example interferometric data set acquired at the Strait of Messina is presented to illustrate the technique. These data reveal and measure tidal currents flowing through the strait. Coherence times in and around the strait are of the order of 0.1 seconds at L band, which is in agreement with previous estimates and measurements. Considerable structure is observed in the amplitude (standard SAR), phase (Doppler) and coherence time imagery.

# L Introduction

Over the past 20 years or so many models have been put forth concerning microwave sensing of the ocean surface. Modulation of the small gravity waves, which radars are sensitive to, have provided oceanographers with the ability to measure the effects of various ocean processes and air/sea interactions. Synthetic aperture radar (SAR) has been one of the most useful tools in this investigation. The time scale at which the scattering remains coherent is particularly important to SAR since the imaging relies on coherent integration to achieve along-track resolution. The same processes and interactions which provide the radar image modulation will also effect the coherence of the surface. If measured over a large scale and at sufficient resolution, the coherence time can provide important insight into many oceanographic phenomenon, especially when paired with the associated backscatter and Doppler imagery such as that provided by an along-track interferometric SAR., Previous measurements of the ocean coherence time have been made using real aperture radars such as that described in [1], however, they lack the synoptic view an airborne or spaceborne SAR can provide. Some recent estimates of the ocean coherence time at L band have been reported in the literature to be on the order of 0.05 to 0.1 seconds [1, 2,3,].

The along-track interferometric SAR used by JPL [4] to measure ocean surface "velocities" makes a direct measurement of the coherence of the ocean surface. This is accomplished by acquiring two complex SAR images in identical geometry, separated by a short time interval, The time interval and identical geometry are obtained by displacing two antenna phase centers forward and aft along the body of the aircraft. The forward phase center images a point on the ocean at a time slightly ahead of the aft phase center. After suitable SAR processing, the correlation between the two complex images is a direct measure of the ocean decorrelation process.

Previously, one antenna has been used to transmit and receive, while a second passive antenna displaced along-track would receive. A technique has been devised [5] whereby measurements at two baselines, or lag times, may be acquired simultaneously with the existing JPL AIRSAR two antenna system by taking advantage of the multi-channel transmit and receive capability required for polarimetric data acquisition. The AIRSAR polarimeter acquires full polarization information by transmitting H and V alternately while receiving H and V from each transmit event, Using an identical scheme, as shown in figure 1, radar pulses are emitted from the forward (F) and aft (A) antennas alternately and received by both. This produces four channels of data, FF, FA, AF and AA, where the first letter indicates transmit antenna position and the second indicates receive antenna position on the aircraft, These channels may be processed to imagery analogous to the polarimetric case. Two unique interferometric baselines maybe constructed using these data; one being the separation distance of the antennas and the second being half this distance. While a similar estimate of the coherence time can be made using a single baseline measurement [6], this dual-baseline estimate is significantly more accurate since it provides a second measured point from which a better functional fit may be estimated. The dual-baseline operating method also provides enough information to allow interferometric phase calibration to be performed using the data alone [7]. Previously stationary calibration targets, such as land, were required to determine the zero velocity phase.

In the next section of this paper, the importance and definition of coherence time is presented, Following that, a description of the along-track interferometric (ATI) SAR technique is given. Some results are presented which show the sensitivity of the ATI velocity measurements to various sensor and physical parameters. The dual baseline interferometric technique is then presented along with the straight forward development of equations which allow the coherence time to be estimated directly using this data. Finally, example data is presented illustrating the techniques described, followed by some conclusions.

## IL Coherence Time

Imaging radars are used quite successfully for a variety of remote sensing applications [8]. Virtually all imaging radars resolve features in the range dimension in the same manner. The distance to a target, or range, is determined by measuring how long it takes a transmitted pulse to travel to the target and back to the radar. Pulses of high bandwidth are used to resolve targets in range. The cross-range (azimuth) resolution, however, is achieved using several different techniques. The simplest imaging radar is a *real aperture radar,* or *RAR. This* kind of non-coherent radar relies on the beam width of the antenna to resolve targets in azimuth. The actual azimuthal positions of the targets within the beam are not known. Most RARs tend to be high-frequency systems, since for a given antenna size, the beam width (and hence resolution) is proportional to the wavelength. Synthetic aperture radar, on the other hand, takes advantage of the fact that as a coherent radar illuminates a stationary ground target while flying by, the phase history of the return pulses will be determined by the geometry. If the data are recorded in such a manner that the phases of the returns are preserved, then increased resolution in the azimuth dimension can be obtained by correcting for the phase variations. This phase correction technique is generically called *azimuth focusing,* and is quite analogous to the action of an optical lens.

While SAR, with its improved azimuth resolution, is a favored radar imaging technique for many applications, it suffers from some peculiarities associated with the azimuth focusing. If some targets are moving against a stationary background, the phase prediction required by the processor will be in error causing the targets to be unfocused and imaged in the incorrect positions, If the phase of the targets varies in any manner not accounted for by the processor focus settings, distortion and azimuth resolution degradation will occur. If the variation is statistically random, some very fundamental limitations will be placed on the quality of the imagery as described by Raney [9].

It is this last point that is of great importance when imaging the ocean with SAR. Because the ocean is not a stationary target, care must be taken when attempting to focus an image. Scatterers on the ocean surface, whether considered patches of long lived Bragg waves or "ping-pong balls," are moving due to a variety of factors including wind, currents, and the action of long waves. The dominant scatterers within a particular resolution cell will in general not remain stationary, or even remain the same physical scatterers. Recent literature abounds with suggested "best" methods for focusing moving ocean waves [10, 11, 12]. I will not address any of the specific arguments, beyond mentioning the recognized importance in all these theories and arguments of the coherence time of the surface.

The coherence time is the time for which the phase of the returns from a resolution cell may be predicted accurately. For a stationary target of known geometric and dielectric properties (and high enough SNR) the coherence time is infinite. Any target that has a coherence time longer than the illumination time, or *integration rime,* of a particular SAR may be considered a coherent target. Most applications involving SAR assume, justifiably, that imaged targets are coherent targets. This allows one to achieve resolutions very close to the theoretical limit. For imaging the ocean, however, this may be far from true. It has been shown by Raney [9] that to process partially coherent data optimally, one requires knowledge of the coherence time. If the coherence time of the ocean is less than the integration time of the SAR, then the realizable azimuth resolution will be limited. Figure 2 shows an example of the JPL AIRSAR L band system azimuth resolution over a range of reasonable coherence times. Notice that the typical SAR image quality of having azimuth resolution being independent of range (or incidence angle) is not true when imaging partially coherent surfaces. Data from this system is presented later in this paper,

The coherence time, $\tau_c$, is defined as the time it takes the auto-correlation function of the complex backscatter field to fall to $1/e$. A Gaussian decorrelation process is used:

$$\rho(t) = exp\left(\frac{t^2}{\tau_c^2}\right). \quad (1)$$

The dual-baseline technique described here simply provides two measurements (at times greater than $t=0$) of this auto-correlation function. Using the two measurements allows one to solve for $\tau_c$. Notice that a single correlation measurement using only one baseline together with the trivial correlation measurement of $\rho(t=0)$, also allows one to estimate the coherence time. Small errors in this single measurement, however, will result in larger errors for the estimate due to the significant extrapolation in time required, Marom described this method and its limitations [6].

Signal to Noise Considerations. The finite signal to noise ratios associated with any real system, will reduce the correlation observed and accuracy of phase estimates. It can be shown [13] that the decorrelation, $\delta$, due to a finite uncorrelated SNR of two along track phase centers is given by:

$$\delta = \frac{1}{SNR + 1} \quad (2)$$

where *SNR is* the signal to *uncorrelated* noise ratio, Typically, thermal noise is the dominant uncorrelated noise source. In general, if the two phase centers have different signal or thermal noise levels, this equation must be modified slightly:

$$\delta(SNR_1, r) = 1 - \frac{SNR_1}{\sqrt{(1+SNR_1)(r+SNR_1)}} \quad (3)$$

where $SNR_1$ is the higher uncorrelated signal to noise ratio, and $r$ is the ratio of the higher to the lower signal to noise levels.

Correlated noise is another, less appreciated, source of error in interferometry and polarimetry. In this case the noise sources in the two channels may be strongly correlated to each other and/or the signal, Sources of correlated noise include certain kinds of radio interference and quantization noise. This type of noise can artificial y increase the correlation between the channels and can

produce a bias in interferometric phase estimation. Quantization noise will typically become critical in low *SNR* (low backscatter) data sets. The effects of correlated noise will not be discussed or considered further in this paper,

## 111. Along-Track Interferomet ry

The technique of using along-track interferometric SAR to measure ocean surface phenomenon was first reported by Goldstein and Zebker of JPL in 1987 [14], This technique requires producing two complex SAR images separated in time, but identical in geometry. The JPL approach has been to use two antennas mounted on the forward and aft side portions of a single aircraft. The JPL AIRSAR system [15] is a three frequency, quad-pol synthetic aperture radar which is flown aboard the NASA DC-8 aircraft, In addition to the standard quad-pol modes, the radar has several experimental modes, one of which is the along-track interferometer (ATI) mode at L and C bands, Table 1 shows relevant AIRSAR parameters.

The first observation (F) corresponds to the complex image produced from a forward phase center, while the second observation (A) is produced from an aft phase center. The aft observation of a particular point on the surface will occur at a time $\tau$ after the forward observation, where $\tau$ is called the *lag time.* Since the geometry is identical, any differences in the two images may be accounted for by changes in the scattering field between the two observation times. By constructing an interferogram, these differences maybe quantified:

$$\Delta\phi = \text{tan-l}\left(\frac{imag(C)}{real(C)}\right) \tag{4}$$

where C corresponds to the interferogram calculated:

$$C = F\,A^{*}. \tag{5}$$

A multi-look phase is determined by coherently summing the nearby interferogram pixels in a filtering process retaining the resultant phase. This method has been shown by Rodriguez [ 16] to be the maximum likelihood estimator for determining the interferometric phase,

Interpretation of the phase measurement is not always straight forward. For moving “hard” targets, the phase difference may be directly interpreted as a possibly ambiguous measurement of the target radial velocity as follows:

$$u = \Delta\phi \frac{\lambda v}{4\pi B} \tag{6}$$

where $\Delta\phi$ *is* the observed phase change, *B* is the baseline length, v is aircraft speed and $\lambda$ is the radar wavelength, The ratio of *B/v* is recognized to be the time lag $\tau$. This interferometer velocity represents the radial component of the phase change. To project this onto the ground image plane, to extract the surface component, one must divide by $sin(\theta)$, where $\theta$ is the incidence angle. Applying this interpretation directly to imaging the ocean would result in a measurement of a component of the surface current, $u_s$ , by the interferometer:

$$u_s = \frac{\Delta\phi}{k_b \tau} \tag{7}$$

where $k_b = (4\pi/\lambda)\, sin(\theta)$ and is identified as the Bragg wavenumber.

This interpretation, however, is too simplistic, as the motion of ocean scatterers is influenced strongly by a variety of other influences, most importantly, wind generated Bragg waves, in addition to surface currents, A more accurate interpretation of the interferometer phase when imaging the ocean can be shown to be that of the mean Doppler shift, $\langle\omega\rangle$ :

$$\Delta\phi = \tau \langle\omega\rangle. \tag{8}$$

Combined with other information or assumptions about the ocean surface, the mean Doppler shift can lead to information about the actual currents or current modulations.

The amount of decorrelation between the two observations may be calculated as well. The multi look correlation coefficient, $\rho(\tau)$, is given by:

$$\rho(\tau) = \left| \frac{\sum FA^*}{\sqrt{\sum |F|^2 \sum |A|^2}} \right| \tag{9}$$

where the summations are carried out over nearby pixels to obtain a better estimate of $\rho(t)$. This measured correlation coefficient will include the effects of noise or registration problems present in the data in addition to the actual decorrelation due to the finite coherence time of the ocean.

An important step involved in producing the data required for the above calculations is the processing of the raw interferometric data to complex imagery, This is a very important step in any interferometer analysis, especially an aircraft borne interferometer. Small motions of the baseline must be accounted for throughout the processing. In effect, the assumption of *identical geometry* mentioned above must be produced by adjusting each return for the slightly different geometry. This requires a special motion compensation algorithm to adjust the relative phases of the returns so that all aircraft motion effects are removed, The data presented in this paper has been processed with such motion compensation, utilizing a modification of the algorithm described in Madsen [17].

There is also the questions of the "zero phase." Since there are unknown relative delays in the radar, "together with changing baselines due to aircraft motion during acquisition, the absolute phase corresponding to zero velocity is not known. Previously this required calibration targets, such as land, to be present in the scene in order to determine phases correctly. Recently, a method has been developed by Lou and van Zyl whereby the zero phase maybe determined using the data and system calibration parameters alone [7].

## Iv. Parametric Analysis

A simple analysis of the along-track interferometer velocity sensitivity to various parameters can be carried out along the lines presented in [18] for topographic interferometric SARS. Using the following expression for the standard deviation associated with interferometric phase measurements [16],

$$\Delta\Phi_{sd} = \frac{1}{\sqrt{2N}} \frac{\sqrt{1-\rho^2}}{\rho} \qquad (10)$$

where N is the number of independent samples averaged and $\rho$ is the correlation between the individual phase centers, the velocity sensitivity to a number of parameters can be calculated, Equation (9) combined with equations (l), (2) and (6) allow us to plot the curves shown in figures 3, 4 and 5 for an L-band along track interferometer. In figure 3, the standard deviation of the radial velocity determined using the interferometer (6) is plotted against the baseline length (for a platform speed = 210 m/s) for various numbers of looks. In this case, a coherence time is assumed to be 150 msec and the SNR is +25 dB. It shows an order of magnitude improvement in the phase estimate can be gained by increasing the number of looks from 1 to 64. Also from this plot, one observes that there is a "best" baseline, although this minimum is quite broad. The existence of an optimum baseline is obvious from the previous equations: The longer the baseline, the less correlated the interferometric pair are, and therefore the larger the phase uncertainty will be. As the baseline approaches O, however, any decorrelation due to finite SNR (6) will limit the phase

accuracy and hence velocity accuracy. The effect of finite SNR on velocity accuracy is shown in figure 4, while keeping the number of looks constant. Clearly, one wants to keep the SNR above +20 dB if possible.

For both the previous figures, the coherence time of the surface was selected based on observations and measurements previously made, including those in this paper. However, the coherence time can vary significantly, even over small distances, depending on the ambient conditions. In figure 5 the velocity sensitivity of the interferometer to various baselines as a function of surface coherence time is presented. This figure best illustrates the difference between along-track and cross-track interferometry design, such as described in [18], Cross-track interferometry allows one to estimate target elevation using two antennas separated perpendicular to the flight direction [19]. In the cross-track case, the decorrelation process is a geometric process to first order. The characteristic decorrelation length is fixed for a given sensor and geometry and it change little within a scene. For the along-track case, the characteristic decorrelation length is defined by the surface coherence time, and there is a significant range of values this can take on within a single scene.

Phase unwrapping becomes an important issue for many interferometric implementations. This is because all the phases detected in the interferograms contain an unknown number of $2\pi$ factors, and the phase variation within a scene may be larger than $2\pi$. Phase unwrapping typically denotes unwrapping the relative phase values throughout the data set, without necessarily determining the actual relation to a true zero phase. For well behaved interferometric data, two dimensional unwrapping algorithms such as described in [20] will perform acceptably, One potential pitfall in unwrapping ATI phases is the natural discontinuities in phase which may occur due to adjacent regions of ocean being dominated by opposite traveling Bragg waves. Over very short distances (order of meters), the dominant Bragg component may cause effective interferometric velocity jumps $\sim f^{*}\sqrt{\frac{g}{k_b}}$ (in the ground range plane) where g is the acceleration of gravity and $k_b$ is the

Bragg wave number. If the interferometric phase difference due to this Bragg speed is greater than $\pi$, confusion in unwrapping the phase will result. A simple calculation yields to following requirement on the along-track baseline time lag, which constrains the maximum baseline so that the phase change due to approaching and receding Bragg waves is less than $\pi$:

$$\tau < \frac{1}{4}\sqrt{\frac{\pi\ \lambda}{g\ sin(i)}} \tag{11}$$

where *i is* the incidence angle, For example, this limits time lags to 3 lms, 68 ms and 150 ms for C, L and P bands respectively. Equation (10) however, is by no means a hard requirement on along-track interferometry design, If the actual velocity or unwrapped phase is not required from the interferogram, as may be the case in some detection algorithms, or where only the channel correlation value is required, this constraint is not important, Also, a system employing multiple baselines may use shorter baselines which do obey (10) to unwrap longer baselines, (In fact, this is the case for the JPL L-band ATI system where the nominal time lags for the two baselines are 47 and 94 msec.)

## V. Dual-Baseline Technique

The classic two antenna interferometric SAR is operated in a manner whereby one antenna is active and used as a standard SAR, while the second antenna is passive. Two receivers are required to simultaneously record the returns provided by the two antennas. These two channels of data are processed independently to complex SAR images and combined interferometrically as previously described, The interferometric baseline is the along-track distance between the phase centers of each channel. The phase center of the active channel (invoking the "start/stop" approximation) is at the phase center of the active antenna. However, the phase center of the passive channel is located half-way between the phase center of the active and passive antennas.

This last point can be intuitively understood by considering the Doppler shift produced by a stationary target as an interferometric SAR passes by. (It is assumed here that the interferometer antennas are displaced along the flight direction of the SAR to make the analogy more intuitive, however, this does not limit the generality.) For the active radar channel (transmitting and receiving on the forward antenna for example) the Doppler will go through zero when the relative radial velocity between the antenna and the target is zero, i.e. when the target is exactly broadside of the forward antenna. At that moment however, the approaching aft antenna motion will still have a component of velocity toward the target, which will cause a positive Doppler in the passive channel. The Doppler will be zero when the negative Doppler produced from the receding forward transmitting antenna some time later, is exactly canceled by the positive Doppler produced by the still approaching aft receiving antenna. This position will be broadside of the point halfway between the two antennas. This zero Doppler point is the phase center for the passive channel.

A second baseline can be realized if instead to the 2 channel operations described above, the interferometer operates in a 4 channel mode. This is accomplished by transmitting out the forward and aft antennas alternately, while receiving from both all the time, and effectively doubling the system pulse repetition frequency to keep the azimuth sampling rate of each channel unchanged, It is in this same manner that 4 channel SAR polarimeters operate [21]. Just as in the case of the polarimeter, a descriptive name is given to each channel: FF, FA, AF and AA corresponding to *transmit out front, receive out front* for "FF" and so on. In the original two channel case, only FF and FA, or AF and AA are available, As stated before, the interferometric baseline for the FF/FA or AF/AA pair is $D/2$, where $D$ is the physical separation of the antennas. When the AA channel is combined interferometrically with the FF channel however, the interferometric baseline is $D$.

Using this dual-baseline technique, two independent measurements of the interferometric velocity can be made with differing sensitivities. In addition, redundant baselines such as FF/FA and AF/AA may be combined to effectively increase the SNR. Also, since measurements of the

decorrelation process are made at two different lag times, one has the ability to estimate the surface coherence time more accurate] y. Assuming a Gaussian coherence function as shown in (1), the two measurements of the correlation coefficient defined in (8) allow one to write the following expression as an estimate of the coherence time:

$$\tau_c = \sqrt{\cdot \frac{\tau_s^2 + \tau_l^2}{ln\,(\rho_s \rho_l)}} \tag{12}$$

where $\tau_c$ is the coherence time, $\tau_s$ and $\tau_l$ are the short and long lag times respectively and $\rho_s$ and $\rho_l$ *are the* measured correlation coefficients at those baselines.

Decorrelation due to correlated and uncorrelated noise will produce errors in the coherence time estimates. This can be seen clearly when imaging land areas which should contain coherent targets. One can readily observe that areas of low signal to thermal noise ratios, such as shadow regions or very smooth surfaces such as roads, will produce estimates which are much too small. Similar SNR variations on the ocean surface will contaminate any coherence time estimates as well. If the absolute SNR throughout the scene is known, the noise induce decorrelation can be statistically estimated and corrected, This is done by adjusting the correlation coefficient prior to calculating the coherence times. However, in practice, accurately determining the SNR can be difficult. Estimating the SNR induced decorrelation, and the SNR itself, may be done using information provided in the dual-baseline data, The two complex images produced by the AF channel and the FA channel produce a zero length baseline interferogram. Any decorrelation between the two channels, therefore, will be due to noise, This *noise decorrelation* interferogram may be used directly to correct the correlation values found at the other baselines, in addition to providing an estimate of the SNR.

## VI. Example Implementation and Measurements

The operation of the JPL AIRSAR along-track interferometer mode [15] was modified so that dual-baseline data could be recorded at both L and C bands. The nominal lag times are shown in table 1. The modifications required of this system to change from the classic active/passive single baseline mode to the dual-baseline mode were minimal. Since the system was originally designed to operate in a quad-pol mode, the dual-baseline modifications simply involved cable changes so that front and back interferometer channels replaced the H and V polarization channels.

Notice the short baseline (--1 O meters at L band) is close to the optimum length according to figures 2 and 4. The long baseline at L band suffers from being too large to uniquely unwrap the Bragg phases, violating the inequality in (10), however, as mentioned earlier, the short baseline may be used to as a guide in unwrapping the longer baseline phase if necessary. At C-band, both baselines are indeed bounded by the inequality in (10).

As an example data set, data acquired in 1991 by the AIRSAR system while imaging a region including the Strait of Messina in Italy is used. This area has been studied over the past decade using both SEASAT and LANDSAT sensors [22,23,24] and was chosen because of the potentially interesting oceanographic features which might be present, The strait connects the relatively shallow Tyrrhenian Sea (600 meters) to the north to the deeper Ionian Sea (1300 meters) in the south. Since the strait has a minimum width of 4 km and an average depth of only about 85 meters, strong tidal currents flow through the strait. Interesting features, from the point of view of their effects on the coherence time, such as "tagli" (tidal bores), are known to be common in this region. A more complete description of the bathymetry and oceanographic features found in the Strait of Messina may be found in [22].

The date and time of interferometer data acquisition was June 28, 1992 at 11:23 GMT, very close to the time of maximum tidal flow through the strait from the north. The radar was operating in the dual-baseline ATI mode at C and L bands, and the quad-pol mode at P band. A more complete

analysis of this entire data set can be found in [25]. Figure 6 shows the swath imaged during the data take of interest.

In figure 7 the ground range L-band interferometric data are presented The NASA DC-8 aircraft was on a heading of 190 degrees, traveling at approximately 215 m/s. The AIRSAR instrument looks to the left side of the ground track and images from approximately 20 degrees incidence out to 60 degrees. The data were processed to 9 meters resolution in slant range by about 1.5 meters resolution in the along-track direction, Careful motion compensation was applied during processing to track the relative position of each antenna. In constructing the interferogram, the data were averaged over an area of about 650 meters$^2$, producing an interferometric data set with an equivalent number of looks of approximately 50. A standard multi-look SAR image created from the interferogram power (to 0.25 power to reduce the image dynamic range), is shown in figure 7a.

In Figure 7b, the mean Doppler image is shown, which is directly proportional to the measured phase difference as given in (8). The color of the image is coded to indicate the measured mean Doppler shift, while the intensity of the color is proportional to the fourth root of the power in the interferogram defined in (5). The land areas are all blue, which indicates no motion, The ocean areas generally have some other color associated with them. Most of the ocean south of the Strait is dominated by the colors light blue to purple which corresponds to a Doppler shift of -2 to -4 Hz. The largest Doppler shifts are observed in the Strait itself, Corresponding interferometric velocity measurements of up to 1.1 m/s (2.0 m/s ground projected) toward the radar are sensed here. The prediced maximum tidal flow through the strait was 2,1 m/s. Figure 8 shows a velocity cut through the middle of the Strait from near range to far range. Note that the velocity goes to O m/s near 30 degrees incidence. This is to be expected as the current follows the strait which becomes more azimuthal in direction with respect to the radar, and the current is not detectable by this technique.

In the phase image, “tagIi” are more clearly visible than in the amplitude image. Tagli are similar to tidal bores and are areas of increased roughness created by the flow inversion whichoccurs in the strait. The local roughness in a tagli has been compared to that of water being blown by a strong wind. In figure 7b, several tagli are seen to extend between Italy and the Sicilian peninsula. There are three clear tagli signatures seen in figure 8, showing apparent back currents on the order of 0.5 to 1.0 m/s. This is consistent with the fact that the tagli propagate against the current.

Another prominent feature in the phase and amplitude images are the patterns in the water south of the strait. The largest feature is just south of the strait and north of Reggio di Calabria. Here the phase is consistent with surface currents on the order of -2 m/s. Note the direction is away from the radar (opposite of the current in the strait). In fact, the sensed current is consistent with a more or less radial current field centered in the middle of the feature (since the interferometer only measures the radial component). This may be an up-welling feature, similar to ones identified in AVHRR imagery of this same area [25].

Figure 7c shows the coherence time image. This image was determined by measuring the correlation of the surface at time lags of 47 and 94 msec using the dual-baseline technique described previously. A coherence time was assigned to each pixel using (12). In this image, all pixels with coherence times longer than 0.25 seconds are colored white. Notice that the land is mostly white indicating that there is high correlation in both interferometric baselines. The areas of the land that are not white are areas of low SNR, such as shadowed or smooth surfaces. The ocean for the most part shows coherence times smaller than 0.25 seconds, and is consistent with previous measurements and estimates cited earlier. The area to the south of the strait (left half of figure 7c) shows a fairly uniform color corresponding to a coherence time of about 0.070 to 0.100 seconds. In contrast, the region to the north of the strait shows considerable structure, and generally longer coherence times. The strait itself seems to be the most interesting area however.

The tagli in the strait visible in the phase image are also visible in the coherence time image, exhibiting shorter coherence times than the surrounding areas. This is consistent with the view that the water in the tagli is rougher. The tagli coherence times are estimated at 0,080 seconds, in comparison to neighboring areas which show relatively long coherence times of 0.180 to 0.25 seconds. Indeed, there are areas of unusually long coherence times of 0.25 to 0,30 seconds just off the tip of Sicily,

Upon closer examination, even the apparently uniform water south of the strait shows structure in the coherence time image. The boundary of the suspected up-welling features observed in the phase and amplitude images are clearly defined as lines of relatively longer coherence times. In addition, there seems to be some fine coherence time structure associated with these larger features in general,

## VII. Conclusion

In the continuing effort to understand ocean processes and how they effect the larger scale global environment in general, radar remote sensing has been used as an important tool. In order to understand these radar measurements, it is important to be able to understand the time scales associated with the small scale waves which determines the radar scatter. Oceanographic and atmospheric phenomenon will modulate and determine any time scale structures which may be present. A method for estimating the coherence time of the ocean surface using a dual baseline interferometric SAR has been presented here. A parametric study showed the JPL AIRSAR along-track interferometer to be suitable for such an application. Data from this system was used to demonstrate the concept. High resolution coherence time images were constructed of the Strait of Messina in Italy. In addition to the coherence time image, the interferometer phase images allowed the detection and measurement of a strong current flowing through the strait. Evidence of

an up-welling was also presented. The measured coherence time of the ocean varied from 70 to 250 msec, and showed quite a bit of large and small scale structure, particularly near the strait itself. The coherence time measurements are in reasonable agreement with previously reported values at L-band.

## Acknowledgment

Special thanks goes to S. Madsen for the development and implementation of the SAR processing and motion compensation algorithms used to process the data presented here, and to Jakob van Zyl for many helpful suggestions made throughout. The work described in this paper was carried out at the Jet Propulsion Laboratory of the California Institute of Technology, and supported under contracts with National Aeronautics and Space Administration (NASA) and the Office of Assistant Under Secretary of Defense (OSD).

[1] W. Plant and W. Keller, "Evidence of Bragg scattering in microwave Doppler spectra of sea return," *J. Geophys. Res.*, vol 95, no C9, 16,299-16,310, 1990.

[2] D. Lyzenga, "An analytic representation of the synthetic aperture radar image spectrum for ocean waves," *J. Geophys. Res.*, vol 93, no Cl 1, 13,859-13,865, 1988,

[3] D. Kasilingam and O. Shemdin, "Theory for synthetic aperture radar imaging of the ocean surface: With application to the tower ocean wave and radar dependence experiment of focus, resolution and wave height spectra," *J. Geophys. Res.*, vol 93, no Cl 1, 13,837-13,848, 1988.

[4] R. M. Goldstein and H. A. Zebker, "Interferometric radar measurements of ocean surface currents," *Nature,* Vol. 328,20 August 1987.

[5] R. E. Carande, "Dual baseline and frequency along-track interferometry," *IGARSS* '92 *Proceedings,* May 1992.

[6] M. Marom, "Interferometric SAR imaging of ocean surface currents and wavefields," Ph.D. Thesis, Naval Postgraduate School, 1990,

[7] Y. Lou and J. J. van Zyl, "Automatic relative phase calibration of the NASA/JPL AIRSAR system in polarimeter, along-track and cross-track interferometer modes," Submitted to *IEEE Trans. Geosci. Remote Sensing.*

[8] J. C. Curlander and R. N. McDonough, Synthetic Aperture Radar: Systems and Signal Processing, John Wiley and Sons, Inc., 1991.

**[9]** R. K. Raney "SAR response to partially coherent phenomena," *IEEE Trans. Antennas Propagat.*, vol AP-28, pp. 777-787, Nov. 1980.

[10] R. K. Raney and P. W. Vachon, "Synthetic aperture radar imaging of ocean waves from an airborne platform: Focus and tracking issues." *J. Goephys. Res,* vol 93, no. C1O, pp. 12,475-12,486, 1988.

[11] C. Bruning, W. R. Aplers, and J. G. Schroter, "On the focusing issue of synthetic aperture radar imaging of ocean waves," *IEEE Trans. Geosci. Remote Sensing, vol. 29,* pp. 120-128, 1991.

[12] D. Kasilingam, " Comments on 'On the focusing issue of synthetic aperture radar imaging of ocean waves' by C. Bruning, W. R. Aplers, and J. G. Schroter," *IEEE Trans. Geosci. Remote Sensing,* vol *29,* pp. 1013-1014.1992.

[13] F. Li, R. Goldstein, "Studies of multibaseline spaceborne interferometric synthetic aperture radars," *IEEE Trans Geosci Remote Sens.*, vol. *28,* no. 1,1990.

[14] R. M. Goldstein and H, A. Zebker, "Interferometric radar measurements of ocean surface currents," *Nature,* Vol. 328,20 August 1987.

[15] J. J. van Zyl, R. E. Carande, Y. Lou, T. Miller, K. Wheeler, "The NASA/JPL three-frequency polarimetric AIRSAR system," *IGARSS '92 Proceedings,* May 1992.

*[16]* E. Rodriguez and J. Martin, "Maximum likelihood estimation of the interferometric phase from distributed targets," to be published in *IEEE Trans Geosci Remote Sens.*

[17] S. Madsen, H. Zebker, J. Martin, "Topographic Mapping Using Radar Interferometry: Processing Techniques," Submitted to *IEEE Geoscience and Remote Sensing.*

[18] E. Rodriguez, J. M. Martin, 'Theory and design of interferometric synthetic aperture radars," *IEE Proceedings-F,* Vol. 139, No. 2, pp 147-159, April 1992.

[19] H. A, Zebker, *et. al.*, "*The* TOPSAR interferometric radar topographic mapping insturment," *IEEE Trans Geosci Remote Sens.*, vol. **30,** no. 5, 1992.

[20] R. M. Goldstein, H, A, Zebker, and C. L. Werner, "Satellite radar interferometry: two-dimensional phase unwrapping." Radio *Science,* Vol. *23,* pp. 713-720, Jul-Aug, 1988.

[21 ] H. A. Zebker, J .J. van Zyl, and D. H, Held, "Imaging radar polarimetry from wave synthesis," *J. Geophys. Res.*, Vol 91, no. B5, pp. 683-701, Jan, 1987.

*[22]* W, Alpers and E, Salusti, "Scylia and Charybdis observed from space," *J. Geophys. Res.*, Vol. 88, No. C3, pp 1800-1808, February, 1983.

*[23]* V. Artale, D. Levi, S, Marullo, and R. Santoleri, "Analysis of nonlinear internal waves observed by Land sat Thematic Mapper,"J. *Geophys. Res.*, Vol. 95, No. C9, pp 16,065-16,073, September, 1990.

[24]L. Nicolo and E. Salusti, "Field and satellite observations of large amplitude internal tidal wave trains south of the Strait of Messina, Mediterranean Sea," *Ann. Geophysical,* vol *9., 534-539, 1991.*

[25] W. R. Alpers, R. E. Carande and E. Salusti, " Oceanic features observed by multifrequency interferometric synthetic aperture radar in the vicinity of the Strait of Messina," in preparation.

## Figure and Table Captions:

**Figure 1.** Transmit and receive events for acquiring four channels of interferometric data required for dual-baseline interferometry

**Figure 2.** Maximum obtainable azimuth resolution for the AIRSAR L-band radar as a function of ocean coherence time and incidence angle. Expected coherence time at L-band is 0.05 to 0.20 seconds. The maximum resolution obtainable for coherent targets (infinite coherence time) is 1 meter independent of incidence angle.

**Table 1.** Parameters of the AIRSAR instrument including the L and C band along-track interferometer (ATI) parameters. Notice the dual-baseline operations provides two time lags.

**Figure 3.** Expected standard deviation of velocity measurements obtainable using ATI techniques at L-band verses baseline length (lag time) and number of looks. Curves are plotted assuming a +25 dB signal to uncorrelated noise ratio and a coherence time of 0.15 seconds.

**Figure 4.** Expected standard deviation of velocity measurements obtainable using ATI techniques at L-band Vs the signal to uncorrelated noise ratio. A coherence time of 0.15 seconds is assumed, with 16 look averaging.

**Figure 5.** Expected standard deviation of velocity measurements obtainable using ATI techniques at L-band Vs baseline length (lag time) and ocean coherence time. 16 look averaging averaging was assumed and a signal to uncorrelated noise ratio of +25 dB.

**Figure 6,** Map of the Strait of Messina showing the imaged swath. The date of data acquisition was June 281991 around 11:23 GMT

**Figure 7.** The top image, 7a, shows a standard multi-look SAR image (L band) constructed from the aft channel of the interferometer. The aircraft was flying from right to left, and near range is at the top of the image. The middle image, 7b, was constructed by coloring the phase difference between the forward and aft processed L band SAR channels. A calibrated color bar is shown in units of interferometric velocity (radial) and mean Doppler shift. The tidal current flowing through the strait from the Tyrrhenian Sea in the North (right) to the Ionian Sea in the South (left) produce the phase shifts obvious in this image. Just to the south of the strait, evidence of a possible upwelling is seen. (The phase wraps around in this region.) The bottom image, 7c, is the corresponding coherence time image produced using the dual baseline interferometric technique. The color mapping used goes from blue to green to yellow to red to white linearly over a time scale of O to 250 milliseconds. Coherence times greater than 250 milliseconds are saturated at white.

**Figure 8.** Plot of the measured velocity along a cut through the strait inferred from the data shown in 7b. In the near range, the velocity goes to zero due to the fact that the current direction becomes azimuthal, to which the along-track interferometer is not sensitive. A maximum current of 2 m/s is observed. "Tagli" are evident in this cut, as regions of slower currents,

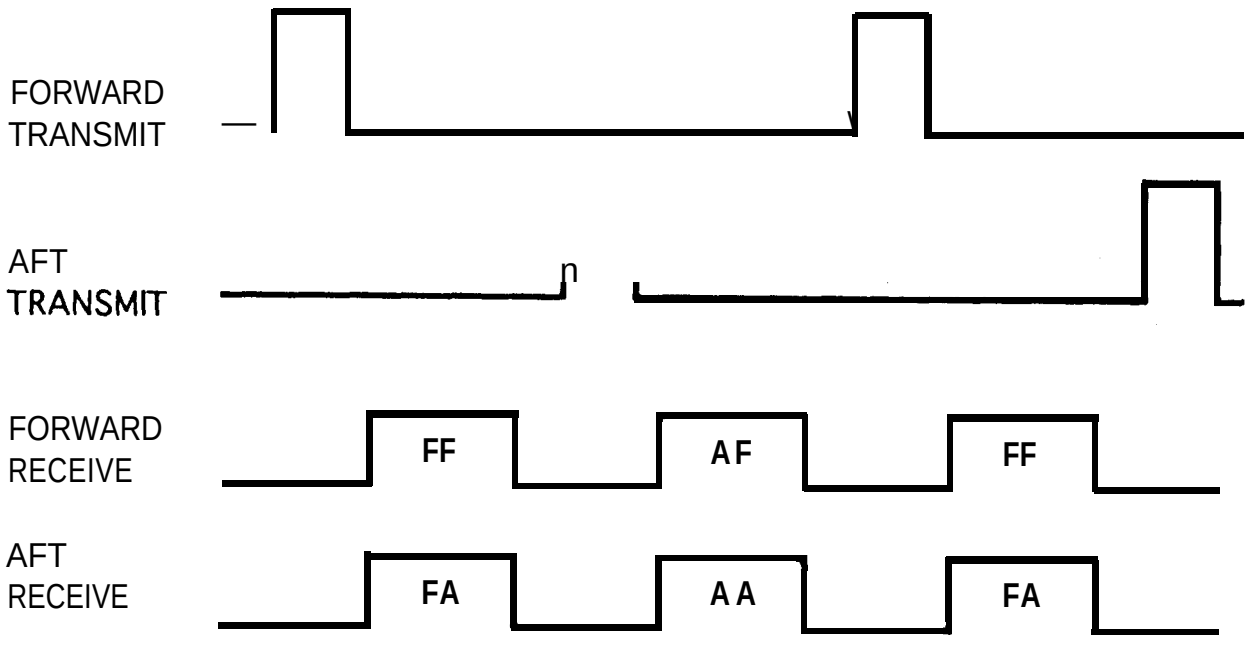


Figure 1. Carande 1993

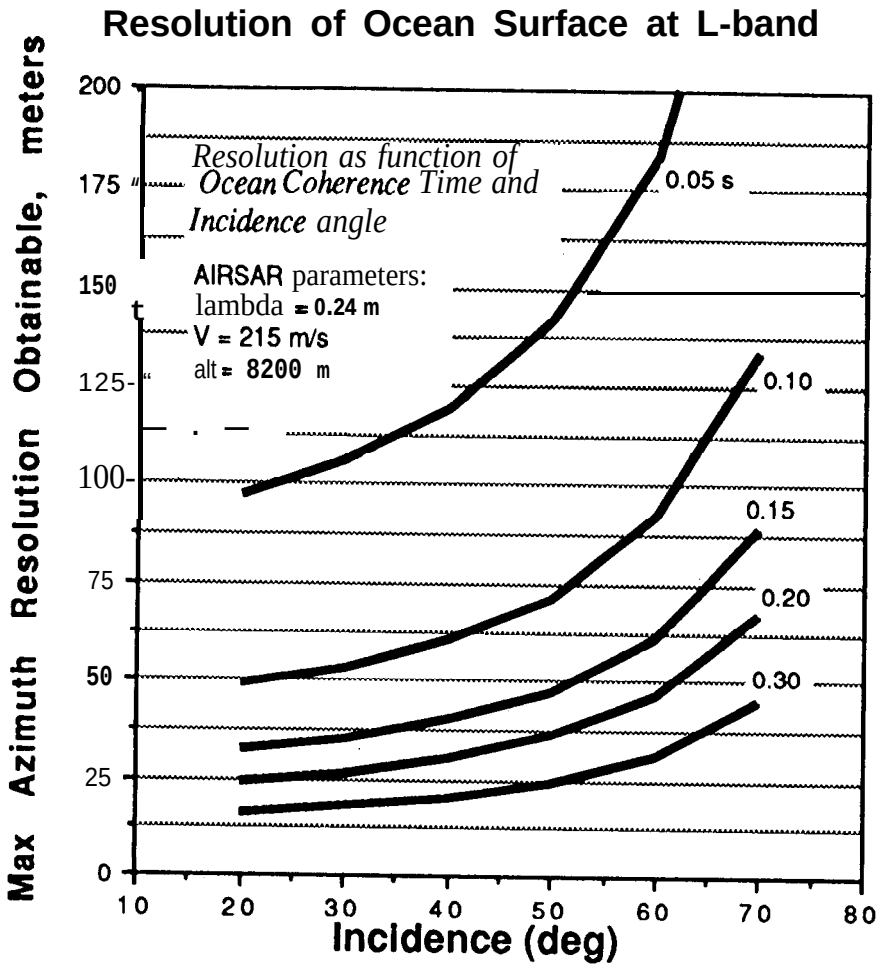


Figure 2. Carande 1993

| Parameter | C-Band | L-Band | P-Band |
|---|---|---|---|
| Center Frequency, MHz | 5298.75 | 1248.75 | 438.75 |
| Wavelength, m | 0.05 | 0.24 | 0.69 |
| Peak Power, W | 1000 | 6000 | 1000 |
| Ave. Power, W | 19 | 110 | 19 |
| Az, El Antenna Size, cm | 136x 16.5 | 161 x 45,5 | 183 x91.5 |
| Az, El Beam, degrees | 2,5, 50 | 8,44 | 19, 38 |
| Nominal gain, dB | 23.3 | 18.3 | 14.1 |
| Noise Equivalent SigmaO, dB | -30 to -35 dB | -45 dB | -45 dB |
| Data Modes | Quad Pol, ATI, XTI | Quad Pol, ATI | Quad Pol |
| Pulse length, usec | 10 or 20 | | |
| Bandwidth, MHz | 20 or 40 | | |
| Transmit waveform | chirp | | |
| Nominal altitude, feet | 26,000 | | |
| Nominal speed, m/see | 210 | | |
| A/C quantization, bits/sample | 8 | | |
| Recorder data rate, Mbits/see | 80 | | |
| ATI MODE: | yes | yes | not available |
| polarization | HH or VV | HH or VV | |
| along-track spacing, m | 1.9 | 19,8 | - |
| along-track spacing, λ | 38 | 82 | |
| cross-track spacing, m | 0.9 | 0.0 | . |
| antenna operations | Front: Trans. & Rec. Aft: Trans. & Rec. | Front: Trans. & Rec. Aft: Trans. & Rec. | - |
| nominal lag times, msec | 4.5, 9.0 | 47, 94 | |

Table 1. Carande 1993

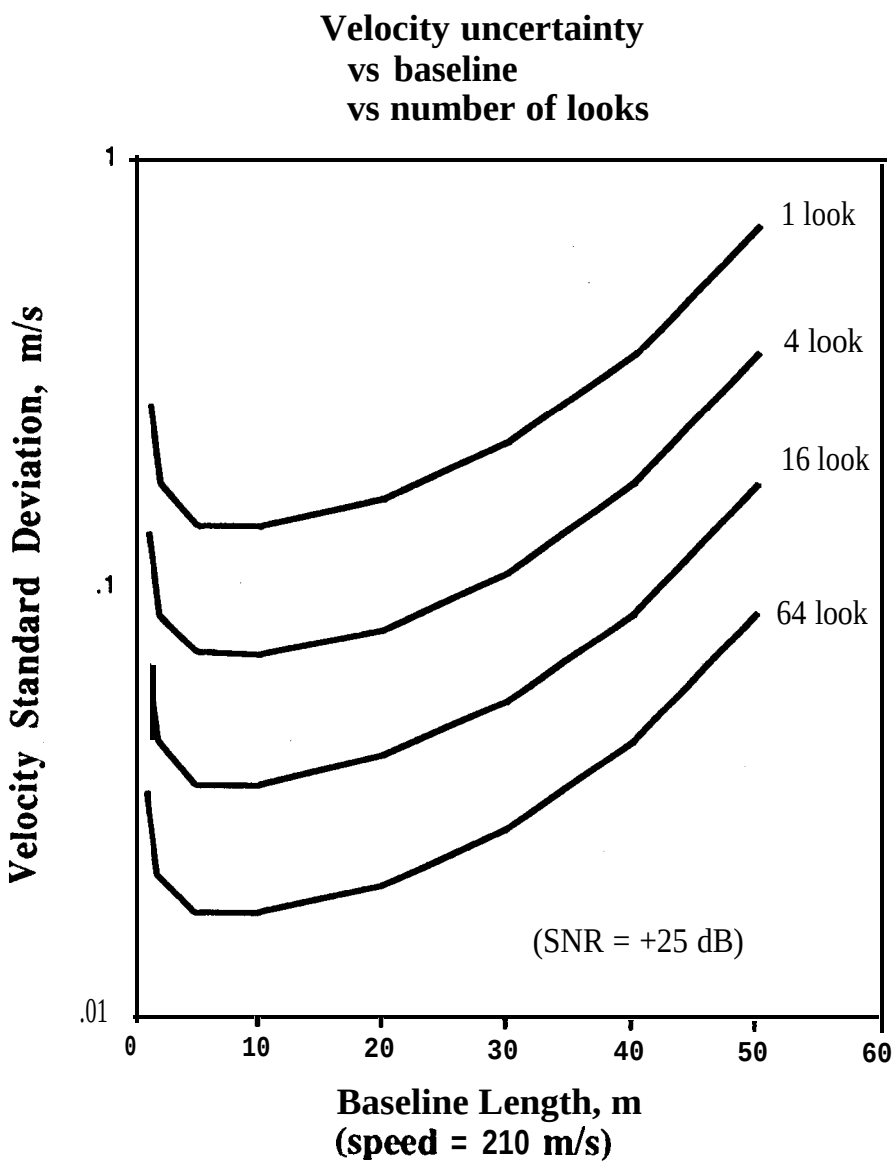


Figure 3. Carande 1993

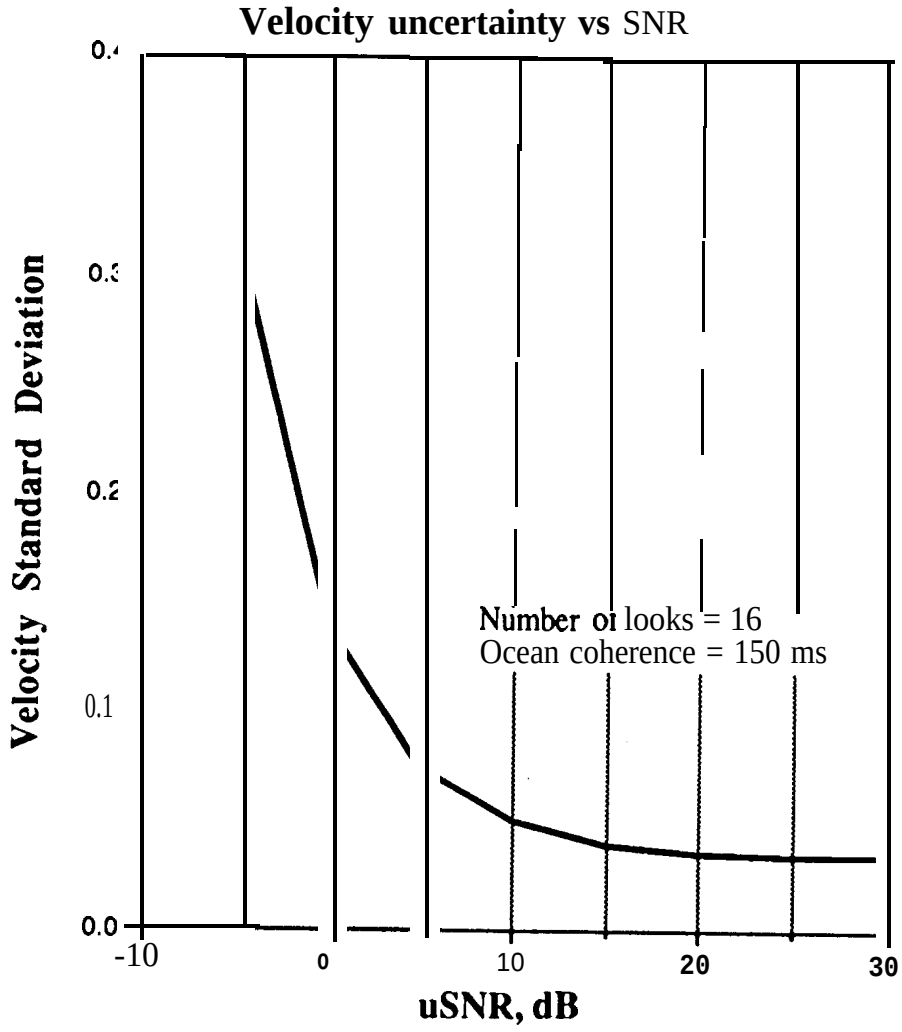


Figure 4. Carande 1993

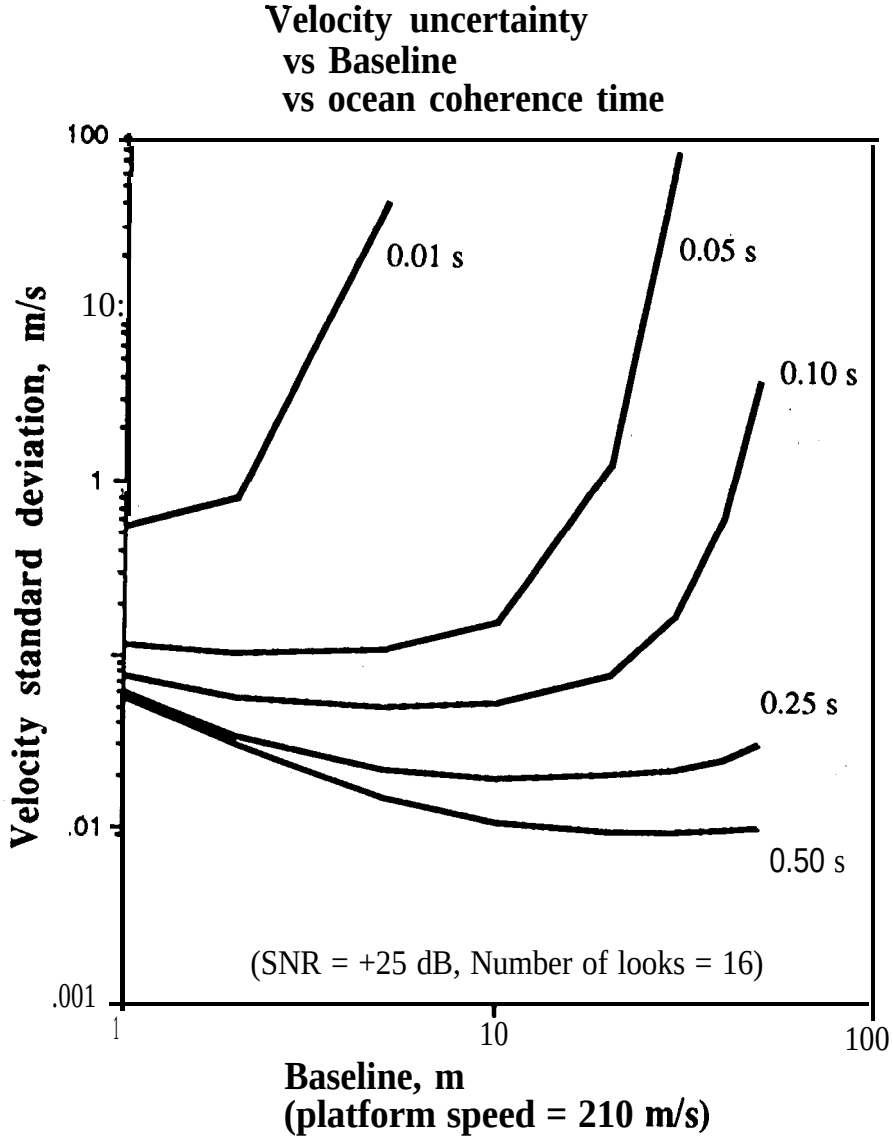


Figure 5. Carande 1993

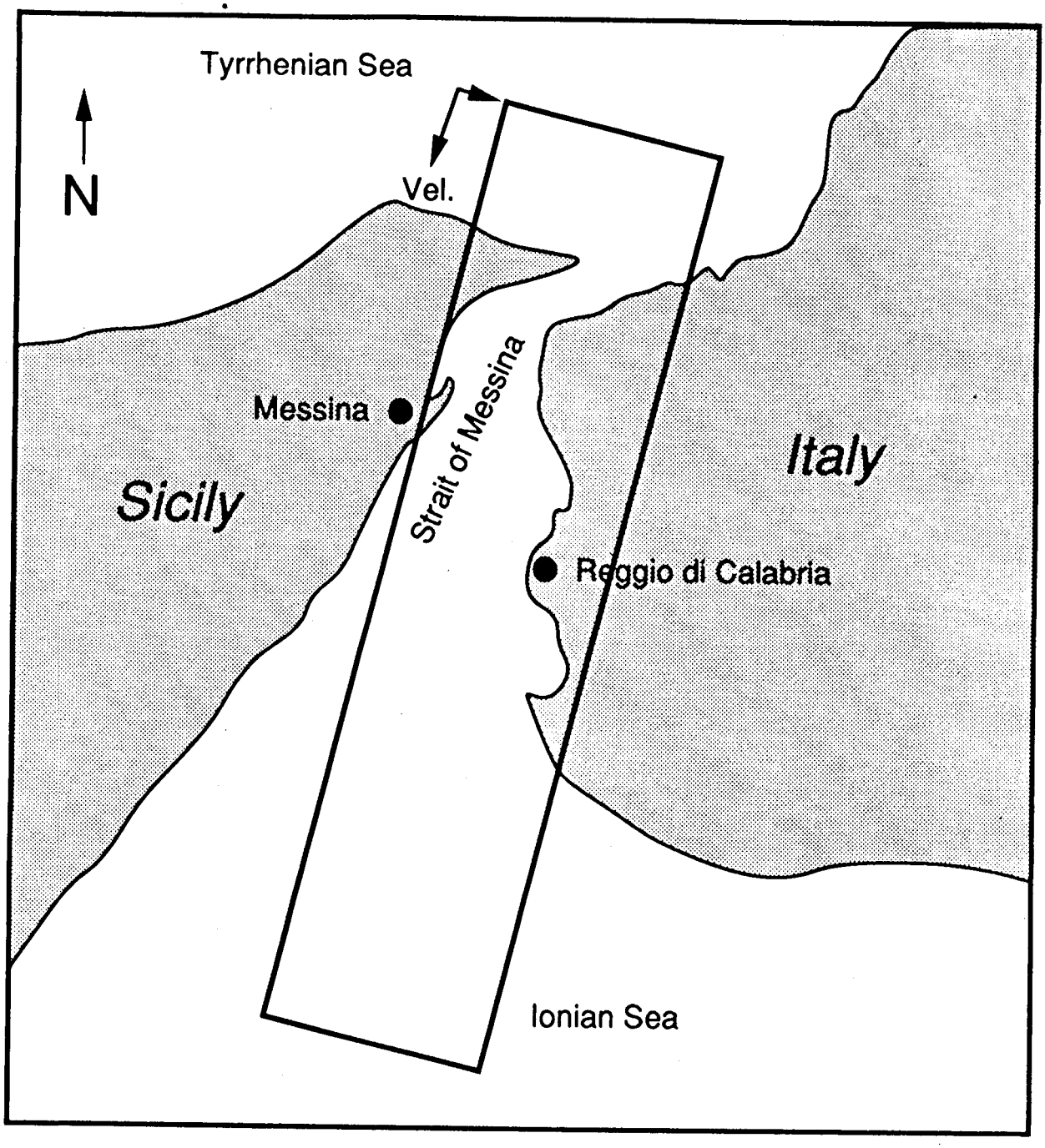


Figure 6. Carande 1993

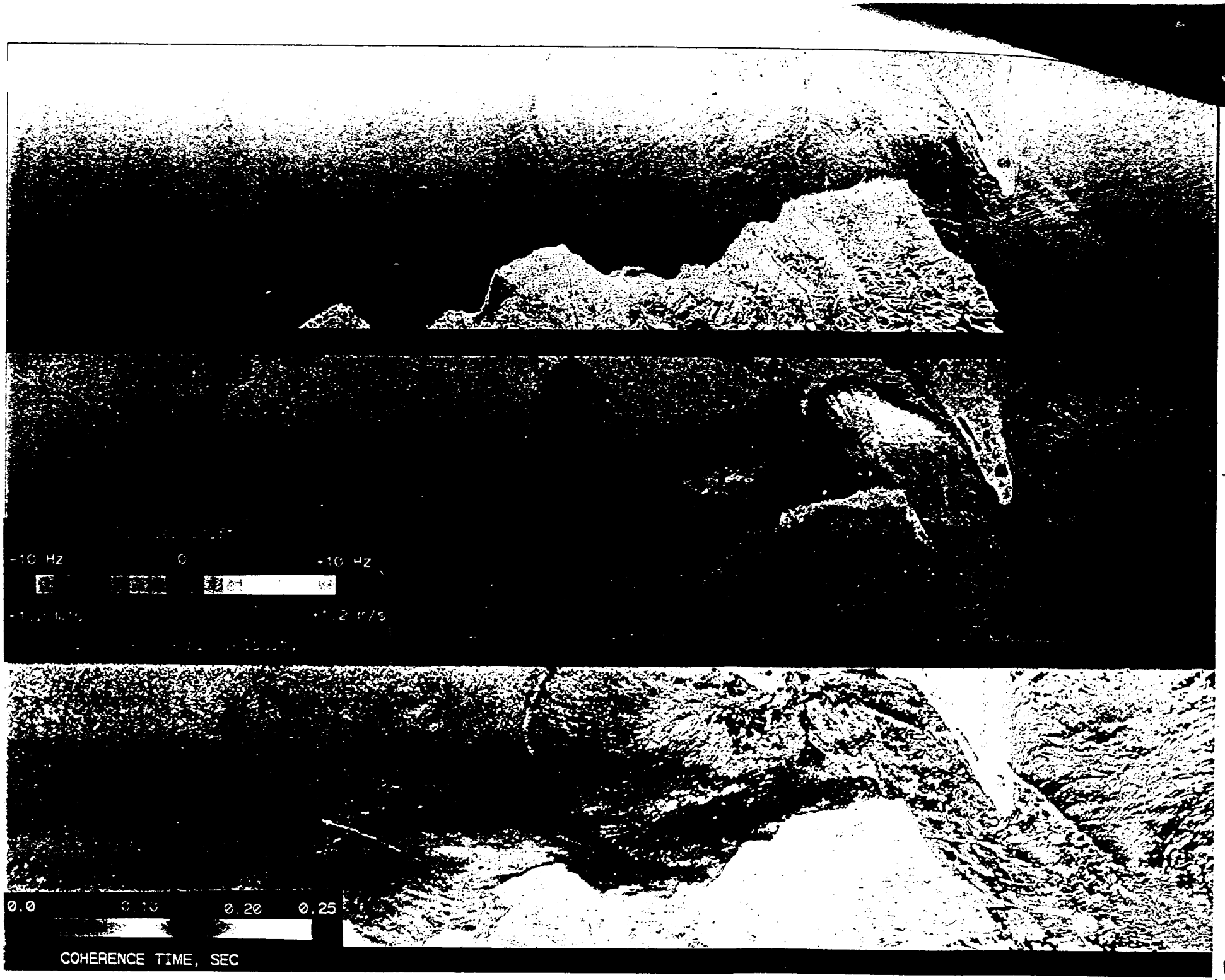


a

b

c

34

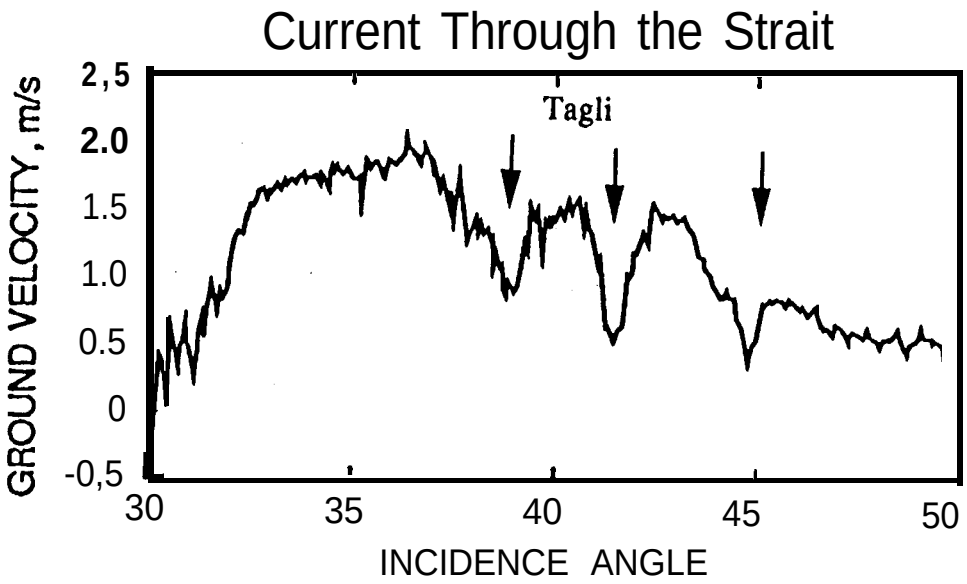


Figure 8. **Carande** 93